ORIGINAL PAPER-EXPLORATION GEOLOGY

Quantitative characterization of pore network and influencing factors of methane adsorption capacity of transitional shale from the southern North China Basin

Wen Liu[1,2] · Qiuchen Xu[3] · Haizhou Wang[4,5] · Peng Liu[6] · Ruiliang Guo[7] · Yang Zhang[4,5] · Keyi Wei[4,5]

Abstract

Quantitative characterization of pore structure and analysis of influencing factors of methane adsorption are important segments in shale gas reservoir and resources evaluation and have not been systematically carried out in marine–continental shale series. A series of integrated methods, including total organic carbon (TOC) contents, Rock-Eval pyrolysis, mineral composition analysis, pore structure measurement, high-pressure CH_4 adsorption analysis and FE-SEM observation, were conducted on 12 transitional shale samples of well WBC-1 in the southern North China Basin (SNCB). The results indicate that TOC contents of the transitional shales range from 1.03 to 8.06% with an average of 2.39%. The transitional shale consists chiefly of quartz, white mica and clay minerals. Interparticle pore, intraparticle pore, dissolution pore and microfracture were observed in the FE-SEM images. The specific surface area (SSA) of BET for the samples ranges from 3.3612 to 12.1217 m^2/g (average: 6.9320 m^2/g), whereas the DR SSA for the samples ranges from 12.9844 to 35.4267 m^2/g (average: 19.67 m^2/g). The Langmuir volume (V_L) ranges from 2.05 to 4.75 cm^3/g (average $= 2.43$ cm^3/g). There is unobvious correction between BET and DR SSA with TOC contents, which means inorganic pores are the main component of pore space in the transitional shale from the SNCB. The relationship of SSA and pore volume shows that micropore has a greater impact on the CH_4 adsorption capacity than mesopore–macropore in the transitional shale. Different from shales in other petroliferous basin, clay minerals are the primary factor affecting adsorption capacity of CH_4 for transitional shale in this study. The pore structure of the transitional shale for this study is characterized by higher fractal dimension and more heterogeneous pore structure compared to shale in other petroliferous basin. This study provides an example and new revelation for the influencing factors of pore structure and methane adsorption capacity of marine–continental transitional shale.

Keywords Shale gas · Transitional shale · Pore structure · Methane adsorption · Southern north china basin

✉ Qiuchen Xu
qiuchenxu@126.com

1 Key Lab of Shale Oil and Gas Geological Survey, Chinese Academy of Geological Sciences, Beijing 100081, China

2 Institute of Geomechanics, Chinese Academy of Geological Sciences, Beijing 100081, China

3 Oil and Gas Survey, China Geological Survey, Beijing 100083, China

4 State Key Laboratory of Petroleum Resources and Prospecting, China University of Petroleum (Beijing), Beijing 102249, China

5 College of Geosciences, China University of Petroleum (Beijing), Beijing 102249, China

6 College of Safety Science and Engineering, Xi'an University of Science and Technology, Xi'an 710054, Shaanxi, China

7 School of Earth Sciences and Engineering, Xi'an Shiyou University, Xi'an 710065, China

Introduction

Shale gas is considered as an important unconventional natural gas resource worldwide (Law 2002). The shale gas can be generated by degradation of kerogen in shale matrix. Generally, self-generation and -storage act as the specific characteristics of shale gas (Zou et al. 2010). The generated shale gas was in different states, including adsorbed gas in micropore and mineral surfaces, free gas in cracking and dissolved gas in crude oil (Martini et al. 1998). Previous studies reveal that the adsorption proportion in shale gas ranges from 20 to 85% (Hill and Nelson 2000). Hence, the adsorption characteristics of shale act as an important leading factor influencing the shale gas accumulation. And investigation of methane adsorption of shale can help to correct evaluation of shale gas resources.

Previous investigations indicate that the adsorption behaviors were closely related to the pore network of shale (He et al. 2019a). The pore can be divided into organic pore and mineral-related pore based on the composition of shale matrix (Zou et al. 2010). Meanwhile, based on the classification of International Union of Pure and Applied Chemistry (IUPAC), three categories of pore consist of the pore network, including macropore, mesopore and micropore. The diameters of them are > 50 nm, 2–50 nm and < 2 nm, respectively. Therefore, the pore in shale is complex and heterogeneous with different pore sizes, pore origins and pore types. Some studies indicate that the pore size can influence the adsorption force between the pore walls and adsorbed gas molecules (Burggraaf 1999; Cao et al. 2020; Chen et al. 2019; Cui et al. 2004; Qiu et al. 2021; Wang and Jin 2019). Generally, the adsorption force decreased with increasing pore width (Burggraaf 1999; Cui et al. 2004). Meanwhile, forming of the organic pore was related to the organic matters in shale, whereas the mineral-related pore has relations with clay, rock-forming and carbonate minerals in shale. Therefore, the adsorption potential can be joint influenced by TOC contents, mineral compositions and pore network.

Shale gas exploration and exploitation have been made breakthroughs in Wufeng–Longmaxi shale and Yanchang shale (Liang et al. 2017; Liu et al. 2020a, 2018a). Recently, the potential of shale gas resources in the SNCB has been confirmed (Liu et al. 2018b; Tang et al. 2016). The SNCB, with area of 15×10^4 km^2, was characterized by a transitional coal-bearing basin in the central area of China (Dang et al. 2017). The deltaic facies marine-terrigenous shale is of wide distribution in the basin and shale gas exploration achieved significance breakthroughs (Liu et al. 2016). The marine–continental transitional shale in this area, including Upper Shihezi, Lower Shihezi, Shanxi and Taiyuan formations, is of high maturity stage and TOC contents, which is a unconventional natural gas exploration potential target (Wang et al. 2015, 2014).

However, the pore network structure, methane adsorption capacity variation and its main controlling factors of transitional shale in different formations in SNCB are not clear. Meanwhile, previous related studies mostly focused on marine and continental shale series, and there is a lack of case study and systematic research on marine–continental transitional shale samples. Hence, in this study, core samples were collected, TOC contents, rock pyrolysis, mineral composition measurement, pore network analysis and CH$_4$ adsorption analysis were performed. The quantitative characterization of pore structure in different formations was investigated and the main controlling factors of adsorption capacity of CH$_4$ from the transitional shale in the SNCB were analyzed (Fig. 1). The results could help us better understanding the shale gas enrichment mechanism and potential in the SNCB basin and provides an example and new revelation for the influencing factors of pore structure and methane adsorption capacity of marine–continental transitional shale.

Geological settings

Fuyang–Bozhou (FB) area is located around Yanji sag, Niqiuji sag, Wanglou slope and Gucheng lower uplift in the east of Zhoukou depression in SNCB (Fig. 2). The basin straddles the southern part of the North China plate (Kaifeng depression), the fault fold belt at the southern margin of the North China plate (Southern Zhoukou depression, Hefei depression) and the North Huaiyang fault fold belt (Xinyang Basin) (Xu et al. 2003). The main forming periods of SNCB span a long time, leading the basin nature and deforming history relatively complex. The tectonic evolution closely related to the Qinling-Dabie orogenic belt, which can be divided into 6 stages as shown in Fig. 3. Neogene, Paleogene, Permian, Carboniferous, Ordovician and Cambrian strata are developed successively in FB area. From top to bottom, it can be further divided into 3 structural layers: Upper structural layer, mainly including Quaternary Pingyuan Formation, Neogene Minghuazhen Formation and Guantao Formation; Middle structural layer, including Paleogene, Triassic, Permian, Carboniferous, Ordovician and Cambrian strata; Lower structural layer is composed of Precambrian basement, including Archean gneiss and Proterozoic metamorphic rock (Fig. 4) (Yu et al. 2005). The data of outcrop observation, drilling and seismic profiles show that Cambrian–Ordovician, Carboniferous–Permian and Neogene–Quaternary strata are relatively thick and widely distributed, while Triassic, Jurassic, Cretaceous and Paleogene have giant residual thickness but limited distribution

Fig. 1 Workflow for the sequence of the current experimental studies
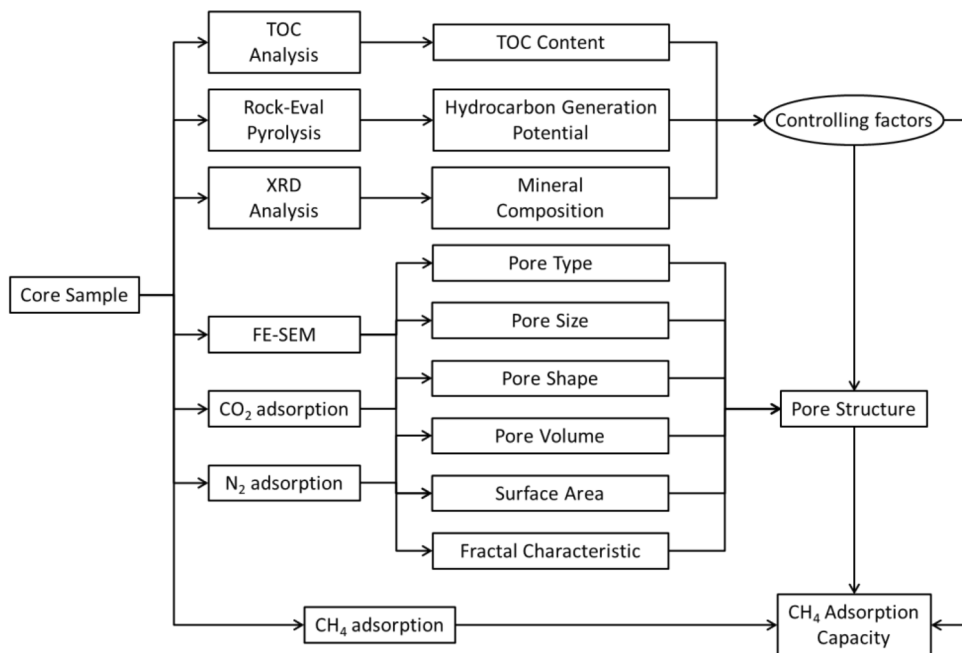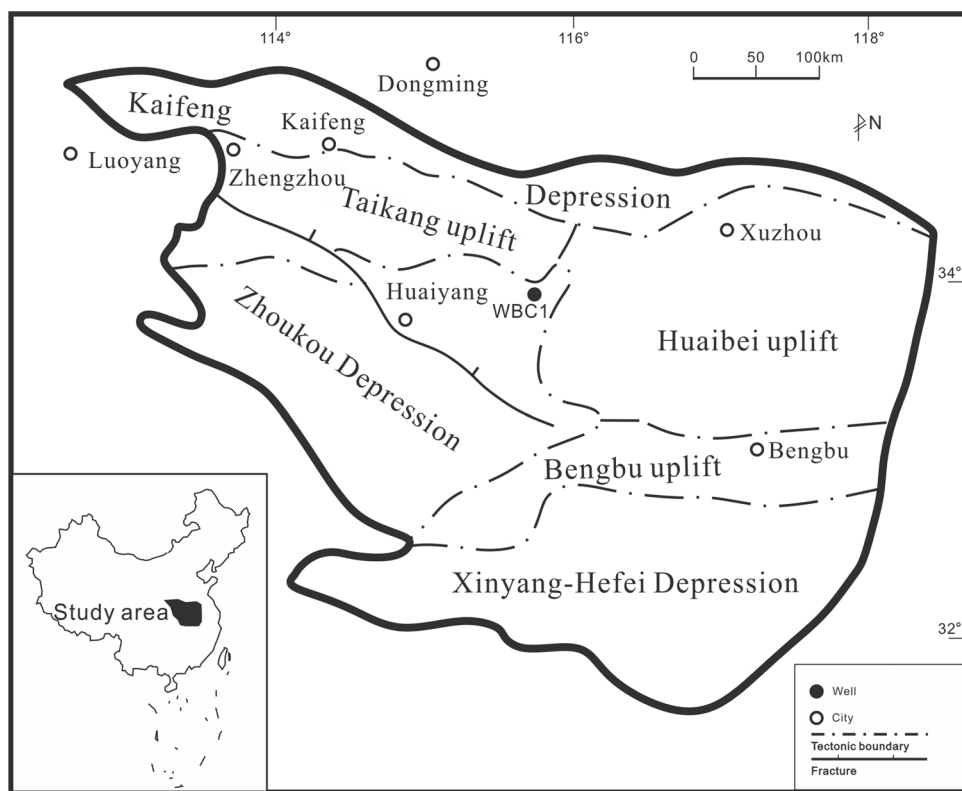

Fig. 2 Maps showing the location of the Well BC-1 in the southern North China Basin

(China Geological Survey) (Anees et al. 2019). Due to the Caledonian movement, the Carboniferous–Permian strata in FB area generally lack the Lower Carboniferous and only have the Upper Carboniferous and Permian, which is mainly a set of marine–continental transitional sandstone, mudstone, carbonates and coal seam strata (Huang et al. 2005). The Carboniferous–Permian strata are deposited continuously and composed of transitional facies clastic rock, mudstone and coal seam.
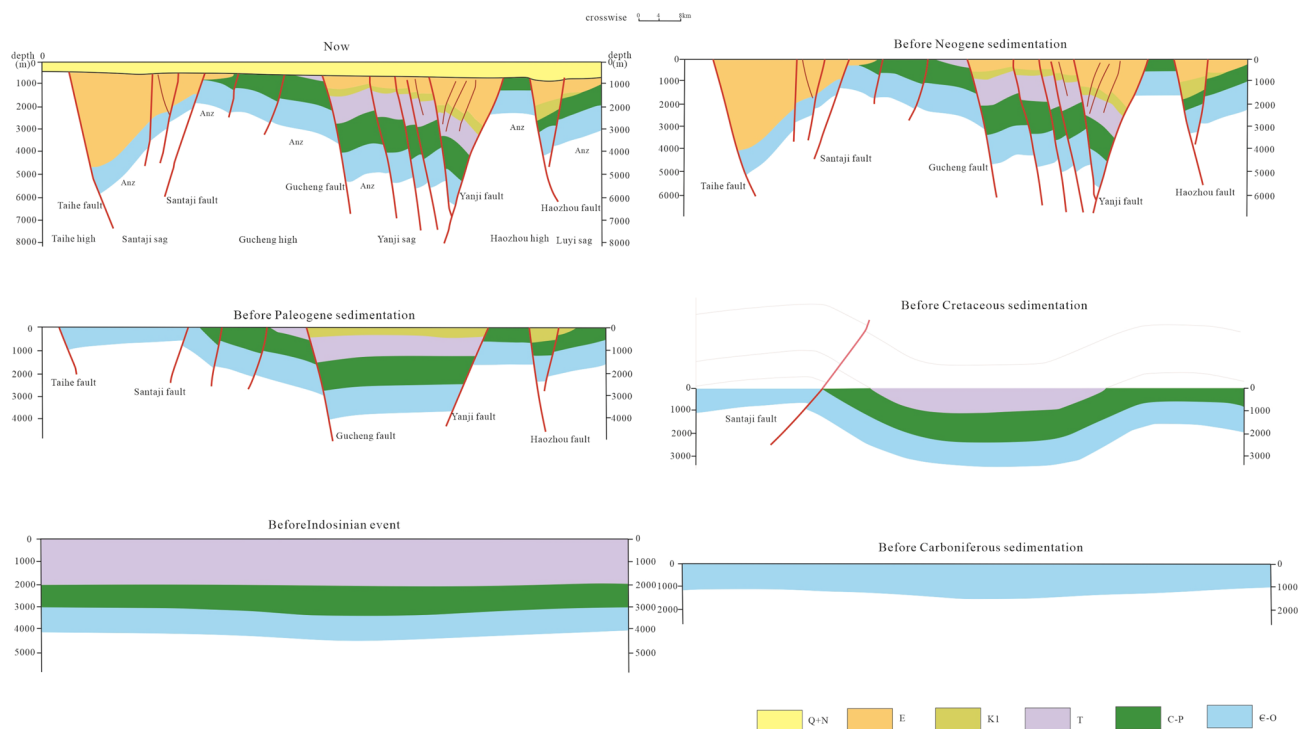
Fig. 3 Tectonic evolution process of the southern North China Basin (Wang et al. 2020)

Samples and experiments

Samples

Twelve core samples were collected from the Permian in Well WBC1, which located in the northern part of the Zhoukou Depression in the basin (Fig. 2). The depths of the collected samples from single borehole WBC1 Well range from 2127 to 2718 m. The lithology of the collected samples was mainly typical gray-black shale or mudstone. The geological information of the samples is presented in Table 1.

Experiments

Total organic carbon (TOC) contents

In this study, the TOC contents were measured by a CS Analyzer (LECO CS-230). Firstly, the samples were crushed to > 100 mesh and excessive HCl was added slowly and then heated at least for 2 h with temperature ranging from 60 to 80 °C. After treated with acid, the sample was put in the porcelain crucible which lay on a nutsch filter and then water-washed until neutral. Finally, the sample was dried with temperature ranging from 60 to 80 °C, then the TOC content was measured and reported as wt%.

Rock-Eval pyrolysis

The rock samples were conduct Rock-Eval pyrolysis experiments by an OGE-II pyrolysis device. In this method, the temperature programmed pyrolysis was applied to shale samples, pyrolysis products at different assigned temperatures were measured and presented as mg/g. In this study, S_1 (the amount of free hydrocarbons in the sample), S_2 (the amount of hydrocarbon generated through thermal cracking of nonvolatile organic matter), T_{max} value (the temperature at which the maximum release of hydrocarbons from cracking of kerogen occurs during pyrolysis (top of S_2 peak) were obtained from the OGE-II pyrolysis device.

Mineral compositions

A X-ray diffractometer (Bruker D8 advance) with a Cu tube was used to determine the mineral compositions. The tube voltage and electric current are less than 40 kV and 40 mV, respectively. The scan ranges from 0 to 140° with a rate of 2°/min and step size of 0.02°.

Pore structure measurement

Low-pressure N_2 and CO_2 adsorption were performed by an ASAP 2020 adsorption apparatus (Micrometrics Instrument Corp., USA) to obtain the pore structure
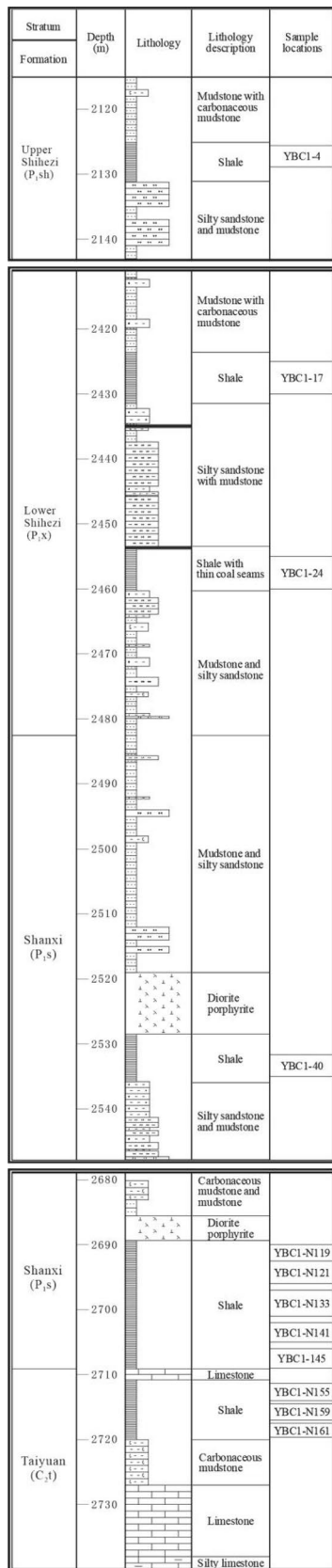
Fig. 4 Stratigraphic column of the marine–continental transitional formations (Wang et al. 2020)

Table 1 Geological information of the transitional shales from Well WBC1 in the southern North China basin

No.	Samples	Depth (m)	Lithology	Formation
1	WBC1-4	2127.7	Shale	Upper Shihezi
2	WBC1-17	2428.2	Shale	Lower Shihezi
3	WBC1-24	2459	Shale	Lower Shihezi
4	WBC1-40	2533.6	Shale	Shanxi
5	WBC1-N119	2692.29	Shale	Shanxi
6	WBC1-N121	2692.99	Shale	Shanxi
7	WBC1-N133	2699.35	Shale	Shanxi
8	WBC1-N141	2703.92	Shale	Shanxi
9	WBC1-N145	2706.41	Shale	Shanxi
10	WBC1-N155	2713.79	Shale	Taiyuan
11	WBC1-N159	2716.74	Shale	Taiyuan
12	WBC1-N161	2718.52	Shale	Taiyuan

characteristics. Low-pressure N_2 adsorption experiment was performed at 77.35 K and the partial pressure (P/P_0) of N_2 ranges from 0 to 1, whereas CO_2 adsorption experiment was conducted at 173.15 K and the partial pressure (P/P_0) of CO_2 ranges from 0 to 0.03. Before the adsorption experiment, ~0.5 g sample with 60–80 mesh was loaded and pretreated at 150 °C for 12 h. Then, the adsorption experiments can be conducted. Based on the experiments, the pore width distribution, specific surface area (SSA) and pore volume (PV) can be achieved by Brunauer–Emmett–Teller (BET) model, Dubinin–Radushkevich (DR) model, Barrett–Joyner–Halenda (BJH) model and density functional theory (DFT) model, respectively.

High-pressure CH₄ adsorption analysis

In this study, the methane adsorption isotherms were measured from 0 to 30 MPa at 60 °C. Firstly, the blank experiments were performed and the volume of the sample tube can be achieved. Then, the sample with 80 mesh was loaded. The sample tube was pumped to less than 10^{-6} MPa and maintained at 105 °C for 4 h in order to remove the water and other gases, which can be adsorbed onto the sample surface. Based on this, the mass of sample can be obtained. Meanwhile, buoyancy measurement was conducted for shale samples with Helium as the carrier gas. The alteration of magnetic suspension balance can be achieved to obtain the buoyancy curve for samples. Therefore, the volume of samples can be obtained by Clapeyron equation. Finally, the sorption measurement was conducted from 0 to 30 MPa at 60 °C.

FE-SEM observation

Five typical samples including WBC1-4, WBC1-N119, WBC1-N133, WBC1-N141 and WBC1-N159 were selected from 12 shale samples to study the microscopic visualization characteristics of pore system and minerals identification. The FE-SEM images of pore morphology visualization were obtained by using a field emission scanning electron microscope (FEI Nova Nano SEM 450). The samples were firstly polished and then prepared by Ar ion beam purging to obtain clear and flat high-magnification images. The secondary electron (SE) images can be achieved at varying magnification of 500× to 10,000×. Meanwhile, the mineral type of specific detrital grains was identified by X-ray energy dispersive spectroscopy (EDS).

Table 2 TOC contents and organic geochemical parameters of the transitional shales from Well WBC1 in the SNCB

Samples	TOC (%)	S_1 (mg/g)	S_2 (mg/g)	T_{max} (°C)
WBC1-4	1.52	0.01	0.08	587
WBC1-17	8.06	0.01	0.18	538
WBC1-24	2.66	0.01	0.09	588
WBC1-40	2.65	0.08	0.04	524
WBC1-N119	2.65	0.03	0.05	431
WBC1-N121	1.59	0.02	0.04	433
WBC1-N133	2.73	0.02	0.06	390
WBC1-N141	1.03	0.01	0.02	450
WBC1-N145	1.42	0.01	0.03	436
WBC1-N155	1.23	0.01	0.03	374
WBC1-N159	1.26	0.01	0.02	386
WBC1-N161	1.89	0.01	0.04	427

Results

Organic geochemical parameters

Organic geochemical parameters for the samples are presented in Table 2. Generally, the TOC contents of the transitional shales are of 1.03–8.06% (average: 2.39%). However, S_1, which represents the amounts of hydrocarbon which can be released as the relatively low pyrolysis temperature (Liu et al. 2019b), is of low values ranging from 0.01 to 0.13 mg/g (average: 0.02 mg/g). Meanwhile, quantification of S_2 parameters during rock pyrolysis indicates the hydrocarbon generated by cracking of organic matters (Liu et al. 2019b). The S_2 in the transitional shales is of 0.02–0.18 mg/g (average: 0.06 mg/g). Generally, the T_{max}–Ro relationship is as follows (Peters et al. 2004):

$$EqV_{Ro} = 0.018 \times T_{max} - 7.16.$$

Based on this, the EqV_{Ro} of the collected transitional shales was calculated, the EqV_{Ro} of the Upper Shihezi and Lower Shihezi shales mainly reveals an over-mature stage. Whereas the samples in Shanxi formation indicate a maturity to over-maturity stage, the samples in Taiyuan formation indicate a low maturity stage.

Mineral composition characteristics

The mineral compositions of the shale samples from Well WBC1 are presented in Table 3. The XRD results reveal that the transitional shale consists chiefly of quartz, muscovite and clay minerals. The contents of quartz range from 3 to 50%, with an average of 33.4%. The contents of muscovite range from 22 to 56% (average: 38.3%). Besides, the clay

Table 3 Mineral compositions of the transitional shales from Well WBC1 in the southern North China basin

Samples No.	Qtz (%)	Fsp (%)	Ms (%)	Clay (%)			Ant (%)	Cal (%)	Dol (%)	Pyr (%)
				Kl	ill	Prl				
WBC1-4	35	2	44	2	11	6	/	/	/	/
WBC1-17	6	2	36	3	23	30	/	/	/	/
WBC1-24	3	2	41	4	30	18	2	/	/	/
WBC1-40	45	3	31	2	14	5	/	/	/	/
WBC1-N119	49	2	24	2	19	4	/	/	/	/
WBC1-N121	41	3	38	2	13	3	/	/	/	/
WBC1-N133	38	2	41	2	13	4	/	/	/	/
WBC1-N141	35	2	46	2	10	5	/	/	/	/
WBC1-N145	50	2	22	3	18	5	/	/	/	/
WBC1-N155	34	2	45	2	14	3	/	/	/	/
WBC1-N159	26	2	52	2	14	4	/	/	/	/
WBC1-N161	39	2	40	2	14	3	/	/	/	/

Note Qtz—quartz; Fsp—feldspar; Ms—muscovite; Kl—kaolinite; ill—illite; Prl—pyrophyllite; Ant—anatase; Cal—calcite; Dol—dolomite; Pyr—pyrite

minerals contents are of 17–56%, with an average of 25.9%, whereas the feldspar and carbonate minerals are of low contents in the transitional shale. Meanwhile, no obvious difference of the mineral composition for the transitional shale from different formations can be observed, may revealing a same depositional environment.

Microscopic characteristics of pore system

Based on the shale pore types classification from Loucks et al. 2012(Loucks et al. 2012), the microscopic pore types of transitional shale samples include interparticle pore (inter-pore), intraparticle pore (intra-pore), dissolution pore (D-pore) and microfracture. Specifically, inter-pores are chiefly slit and polygonal shaped with relatively good connectivity (Fig. 5b). Intra-pores can be further subdivided into nearly parallel slit-like pores inside mineral grains (Fig. 5a, d and f) and disordered inter-crystalline pores associated with clay matrix (Fig. 5a, b and f), in which intra-pores within clay are mostly hosted by I/S mixed layer aggregates and constitute the mainstay of micropores. D-pores are mainly distributed as long slits along the edge of grains and filled with organic matter (OM) mostly (Fig. 5d). Long microfractures that cut through the grains are quite developed (Fig. 5b), together with intra-pores comprised the most prevalent pores in the samples. In addition, organic matter pores (OM-pores) are not developed basically (Fig. 5c and

e), only a few shrinkage pores occasionally occur at the rim (Fig. 5c). Meanwhile, inter-crystalline pores within pyrite are undeveloped also (Fig. 5e).

Low-pressure adsorption isotherms

Types of adsorption–desorption isotherms of N_2 and hysteresis loops

The adsorption isotherms of N_2 represent the relationship of pressure and measured adsorption–desorption capacity, which act as the foundation of calculating the SSA and pore width distribution via BET and BJH model. Besides, the adsorption–desorption isotherms are the only measured data during the low-pressure adsorption experiment of N_2. The adsorption–desorption isotherms of N_2 for the sample are presented in Fig. 6. The results reveal that the isothermal adsorption–desorption curve for samples from Upper Shihezi, Lower Shihezi, Shanxi and Taiyuan present the type II curve shapes based on the classification of Brunauer–Deming–Deming–Teller (BDDT) (Kuila and Prasad 2013). In addition, based on the IUPAC classification of the adsorption hysteresis, the adsorption hysteresis for the tested samples can be distinguished as types H_2 and H_4 (Sing 1982). Meanwhile, some samples show a mixture adsorption hysteresis from H_2 and H_4. The isothermal adsorption–desorption curve and adsorption hysteresis of the transitional shales
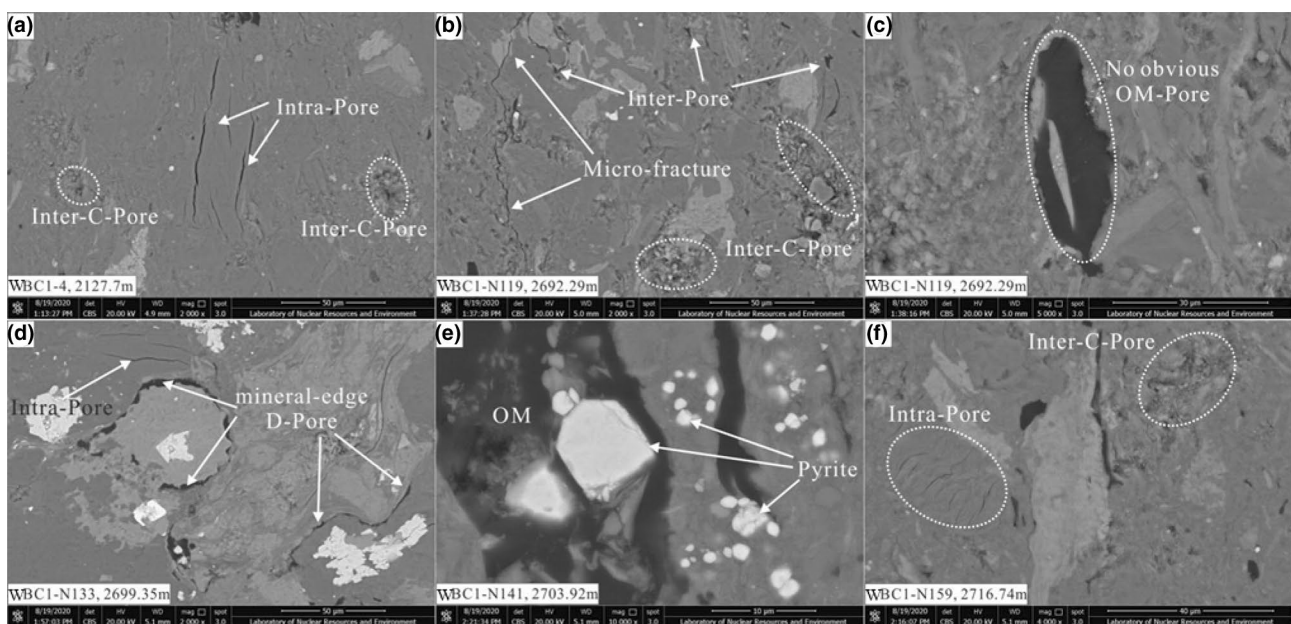

Fig. 5 Pore system microscopic characteristics of the transitional shale samples. **a** Nearly parallel slit-like intraparticle pore (intra-pore) hosted by mineral grains and disordered inter-crystalline pore within clay matrix (inter-C-pore); **b** long microfracture, slit and polygonal interparticle pore (inter-pore) along with inter-C-pore; **c** no obvious organic matter pore (OM-pore) are found; **d** narrow and long dissolution pore (D-pore) distributed along the edge of grains; **e** organic matter (OM) and pyrite aggregates without pore developed; **f** slit-like intra-pore and disordered inter-C-pore
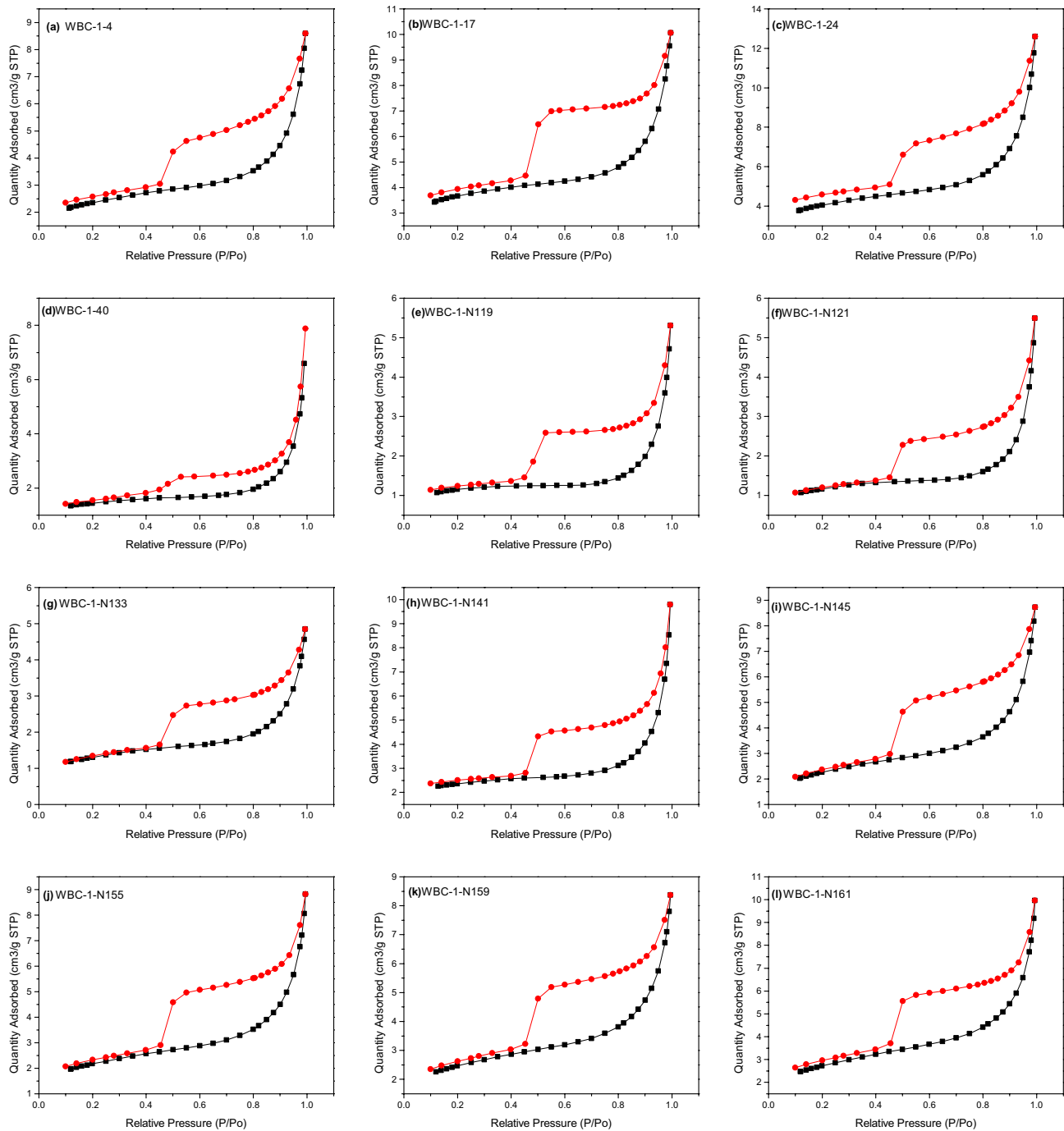
Fig. 6 Adsorption and desorption isotherms of N_2 for the transitional shales from Well WBC1 in the SNCB

indicate that the monolayer adsorption can occur on the surface of the shale matrix. Two inflection points can be observed in the isothermal adsorption–desorption curve during the ascent process, which means that the sub-monolayer adsorption has transferred to the monolayer adsorption and the monolayer adsorption transferred to multilayer adsorption. Moreover, the types of adsorption hysteresis reveal that the shales are characterized by a uniform pore structure

and same cylindrical pore can also contribute to the pore structures.

Adsorption capacity of N_2 and CO_2 for shale

Maximum adsorption capacity of N_2 and CO_2 for shale samples from different formations of SNCB is presented in Table 4. The experimental results show that the maximum

Table 4 Maximum adsorbed N_2 and CO_2 for shale from different formations in SNCB

Samples	Depth (m)	Formation	Maximum adsorbed N_2 cm^3/g	Maximum adsorbed CO_2 cm^3/g
WBC1-4	2127.70	Upper Shihezi	8.5951	2.4433
WBC1-17	2428.20	Lower Shihezi	10.0551	3.0013
WBC1-24	2459.00	Lower Shihezi	12.5993	4.2429
WBC1-40	2533.60	Shanxi	7.8761	1.9854
WBC1-N119	2692.29	Shanxi	5.3033	1.8757
WBC1-N121	2692.99	Shanxi	5.4928	1.2639
WBC1-N133	2699.35	Shanxi	4.8521	2.3214
WBC1-N141	2703.92	Shanxi	9.7950	1.3650
WBC1-N145	2706.41	Shanxi	8.7309	1.9743
WBC1-N155	2713.79	Taiyuan	8.8197	1.9655
WBC1-N159	2716.74	Taiyuan	8.3703	1.6135
WBC1-N161	2718.52	Taiyuan	9.9556	2.1124

Fig. 7 Measured excess adsorbed amount of methane (V_{ex}: ml/g) at P (MPa) for shale from SNCB

adsorbed N_2 (cm^3/g) for all the samples is greater than maximum adsorbed CO_2 (cm^3/g). For shale sample from Upper Shihezi formation, the maximum adsorbed N_2 and CO_2 are 8.5951 cm^3/g and 2.4433 cm^3/g, respectively. The average maximum adsorbed N_2 and CO_2 for Lower Shihezi shales are 11.3272 cm^3/g and 3.6221 cm^3/g, respectively. In addition, the average maximum adsorbed N_2 and CO_2 for Shanxi shales are 7.0008 cm^3/g and 1.7976 cm^3/g, respectively. The average maximum adsorbed N_2 and CO_2 for Taiyuan shales are 9.0485 cm^3/g and 1.8971cm^3/g, respectively. Generally, the shale from the Lower Shihezi formation is characterized by highest value among the different formations.

High-pressure methane adsorption isotherms

In this study, following equation was applied to calculate the actual adsorbed amounts (Gasparik et al. 2012):

$$V_{ex} = V_L \cdot \frac{P}{P_L + P} \cdot \left(1 - \frac{\rho g}{\rho a}\right).$$

V_{ex} represents the excess adsorbed amount at p (MPa). P_L and V_L are the Langmuir pressure (MPa) and the Langmuir volume (cm^3/g), respectively. The measured V_{ex} at different pressure ranging from 0 to 30 MPa is presented in Fig. 7. In this study, the measured V_{ex} of methane was fitted by the above model to describe the adsorption behavior of the transitional shales. The Langmuir pressure P_L (MPa) and the Langmuir volume V_L (cm^3/g) in CH_4 adsorption experiment are listed in Table 5. V_L for 10 samples ranges from 2.05 to 4.75 cm^3/g (average = 2.43 cm^3/g). P_L for 10 samples ranges
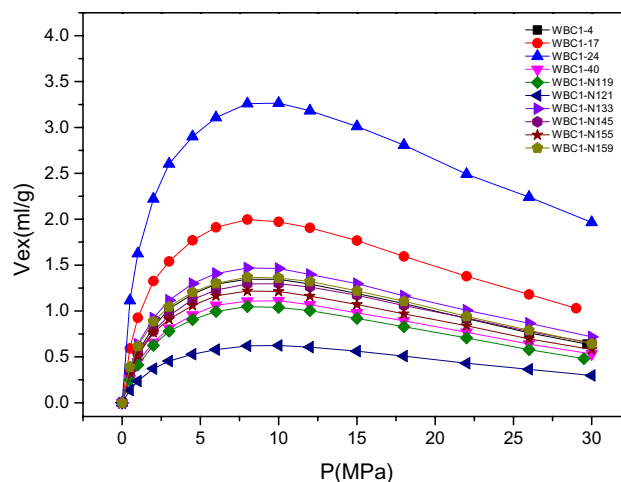
from 2.01 to 3.63 MPa (average = 3.09 MPa). Generally, V_L for shales from Upper Shihezi and Lower Shihezi formations ranges from 2.35 to 4.75 cm^3/g (average = 3.42 cm^3/g), V_L for shales from Shanxi formations ranges from 1.14 to 2.47 cm^3/g (average = 1.94 cm^3/g), V_L for shales from Taiyuan formations ranges from 2.05 to 2.27 cm^3/g (average = 2.16cm^3/g), suggesting that the Upper Shihezi and Lower Shihezi shales are characterized by greatest adsorption capacity of methane among the shale samples.

Discussion

Relationship between SSA and TOC contents and its geological significance

Based on the adsorption–desorption isotherms of N_2, the BET model was applied to obtain the SSA. However, BET

Table 5 Fitted Langmuir pressure and Langmuir volume of the transitional shales from Well WBC1

Samples	Depth (m)	Formation	V_L cm^3/g	P_L MPa
WBC1-4	2127.70	Upper Shihezi	2.35	3.33
WBC1-17	2428.20	Lower Shihezi	3.16	2.53
WBC1-24	2459.00	Lower Shihezi	4.75	2.01
WBC1-40	2533.60	Shanxi	1.97	3.62
WBC1-N119	2692.29	Shanxi	1.88	3.63
WBC1-N121	2692.99	Shanxi	1.14	3.91
WBC1-N133	2699.35	Shanxi	2.47	3.05
WBC1-N145	2706.41	Shanxi	2.24	3.39
WBC1-N155	2713.79	Taiyuan	2.05	3.08
WBC1-N159	2716.74	Taiyuan	2.27	2.86

SSA only can describe the SSA of > 2 nm pore (Liu et al. 2020b). Hence, the features of micropore were obtained from the adsorption isotherms of CO_2. The Dubinin–Radushkevich (DR) model can be applied to obtain the SSA of < 2 nm pore. The BET and DR SSA are presented in Table 6. In general, the BET SSA for the samples ranges from 3.3612 to 12.1217 m^2/g (average: 6.9320m^2/g). The DR SSA for the samples is of 12.9844–35.4267 m^2/g, with a mean of 19.67 m^2/g. The results show that the DR SSA is greater than BET SSA in all samples. Meanwhile, the BET and DR SSA show different characteristics among four formations. In general, the Upper Shihezi and Lower Shihezi shales are characterized by higher specific surface area compared to Shanxi and Taiyuan shale.

Table 6 Specific surface area (SSA) of the transitional shales from Well WBC1

Samples	Depth (m)	Formation	BET SSA m^2/g	DR SSA m^2/g
WBC1-4	2127.7	Upper Shihezi	7.3279	22.5739
WBC1-17	2428.2	Lower Shihezi	10.8256	25.8123
WBC1-24	2459	Lower Shihezi	12.1217	35.4267
WBC1-40	2533.6	Shanxi	4.3277	20.4935
WBC1-N119	2692.29	Shanxi	3.3612	18.6696
WBC1-N121	2692.99	Shanxi	3.5944	12.9844
WBC1-N133	2699.35	Shanxi	4.1465	20.7379
WBC1-N141	2703.92	Shanxi	6.8267	12.0857
WBC1-N145	2706.41	Shanxi	7.2521	17.6027
WBC1-N155	2713.79	Taiyuan	6.9427	17.1972
WBC1-N159	2716.74	Taiyuan	7.7223	14.0413
WBC1-N161	2718.52	Taiyuan	8.7342	18.3796

Figure 8a shows the relationship of BET and DR SSA with TOC contents of the samples. The results reveal that unobvious correction can be discovered between BET and DR SSA with TOC contents. Accordingly, the R^2 of the linear regression for BET and DR SSA with TOC contents is only 0.13 and 0.27, respectively. In addition, the correction of TOC contents and maximum quantity adsorbed N_2 and CO_2 are presented in Fig. 8b, the results indicate that the maximum quantity adsorbed N_2 and CO_2 show an unobvious positive correction with TOC contents. The experimental results reveal that the micropore, mesopore and macropore in the transitional shales may mainly be contributed by inorganic pore. However, compared with the relationship of BET SSA and maximum quantity adsorbed N_2 with TOC contents, better corrections of DR SSA and maximum quantity adsorbed CO_2 with TOC contents can be observed in this study, indicating that organic pore contributes more micropore in shale compared with mesopore and macropore. The FE-SEM images can further support this understanding. The pore space of transitional shale samples is mainly composed of intra-pore and microfracture. OM-pores are undeveloped basically, just a few shrinkage micropores and slits distributed at the edge of OM, and these pore spaces belong to the category of micropore (Fig. 5c).

Comparison of pore width distribution characteristics of shale from different formations

Figures 9 and 10 show the SSA and PV distributions for the shale samples from transitional shale of SNCB, which was obtained from BJH model. Based on this, the SSA and PV of micropore, mesopore and macropore can be obtained and the results are presented in Table 7. Generally, SSA of
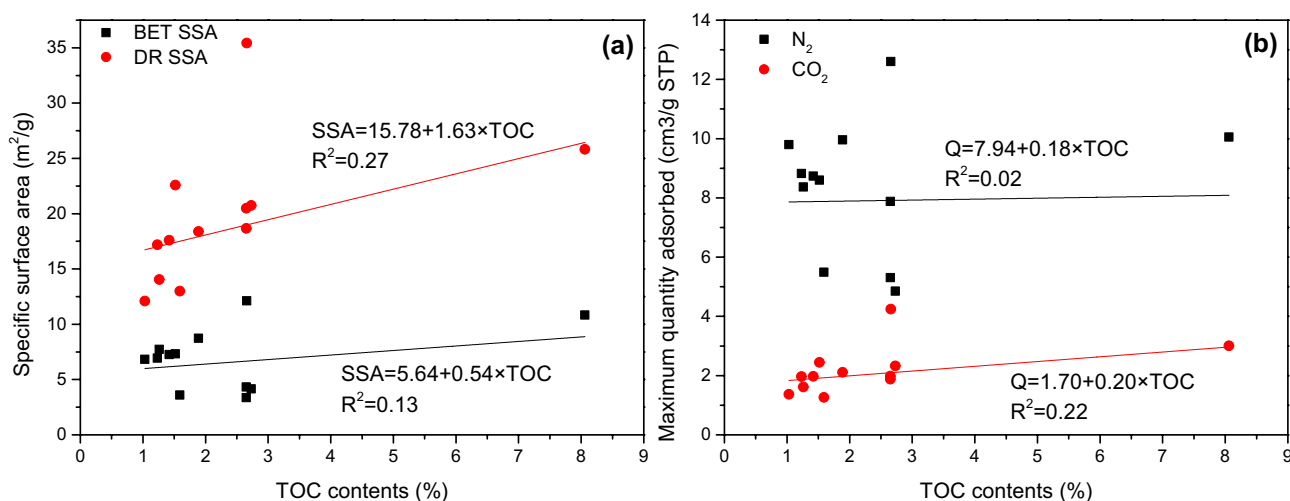

Fig. 8 Relationship of specific surface area **a** and maximum quantity adsorbed gas **b** with TOC contents of the shale samples

micropore in shale from Lower Shihezi Formation ranges from 8.5894 to 14.9121 m²/g (average = 11.7508 m²/g). However, average SSA of micropore of shale in Upper Shihezi, Shanxi and Taiyuan Formations is 3.8602 m²/g, 3.9124 m²/g and 3.9031 m²/g, respectively, while the average SSA of mesopore in shale from Shanxi Formation is 1.1565 m²/g, which is less than samples from other formations. But, no obvious difference can be discovered in SSA of mesopore in the samples. Meanwhile, the PV in the samples shows similar characteristics. Hence, the results indicate that the shale in Lower Shihezi Formation is characterized by the greatest SSA. Moreover, relative percent of micropore of shale from Shanxi Formation is the highest among the shale samples of four formations (Fig. 11).

Heterogeneity of pore system

It is widely acknowledged that fractal dimension can describe the irregularity of pore structure and evaluate the complex shapes in shales (Cao et al. 2016; Guo et al. 2020; Mangi et al. 2020; Xi et al. 2018; Yang et al. 2016b). Heterogeneous shale pore network can be quantitatively characterized by fractal dimension (Pfeifer and Avnir 1983). Previous studies have proposed different methods and models to obtain fractal dimension, including fractal Frenkel–Halsey–Hill (FHH) model, Langmuir model, thermodynamic model, fractal BET model and MIP (Avnir and Jaroniec 1989; Jaroniec 1995; Rouquerol et al. 1994). Among above methods and models, FHH model is considered as the most effective approach to obtain the fractal dimension and describe the irregular geometry of pore structure of shale (Shang et al. 2020; Sun et al. 2016; Xu et al. 2020). The FHH fractal dimension can be directly obtained from N₂ adsorption and can be described as follows:

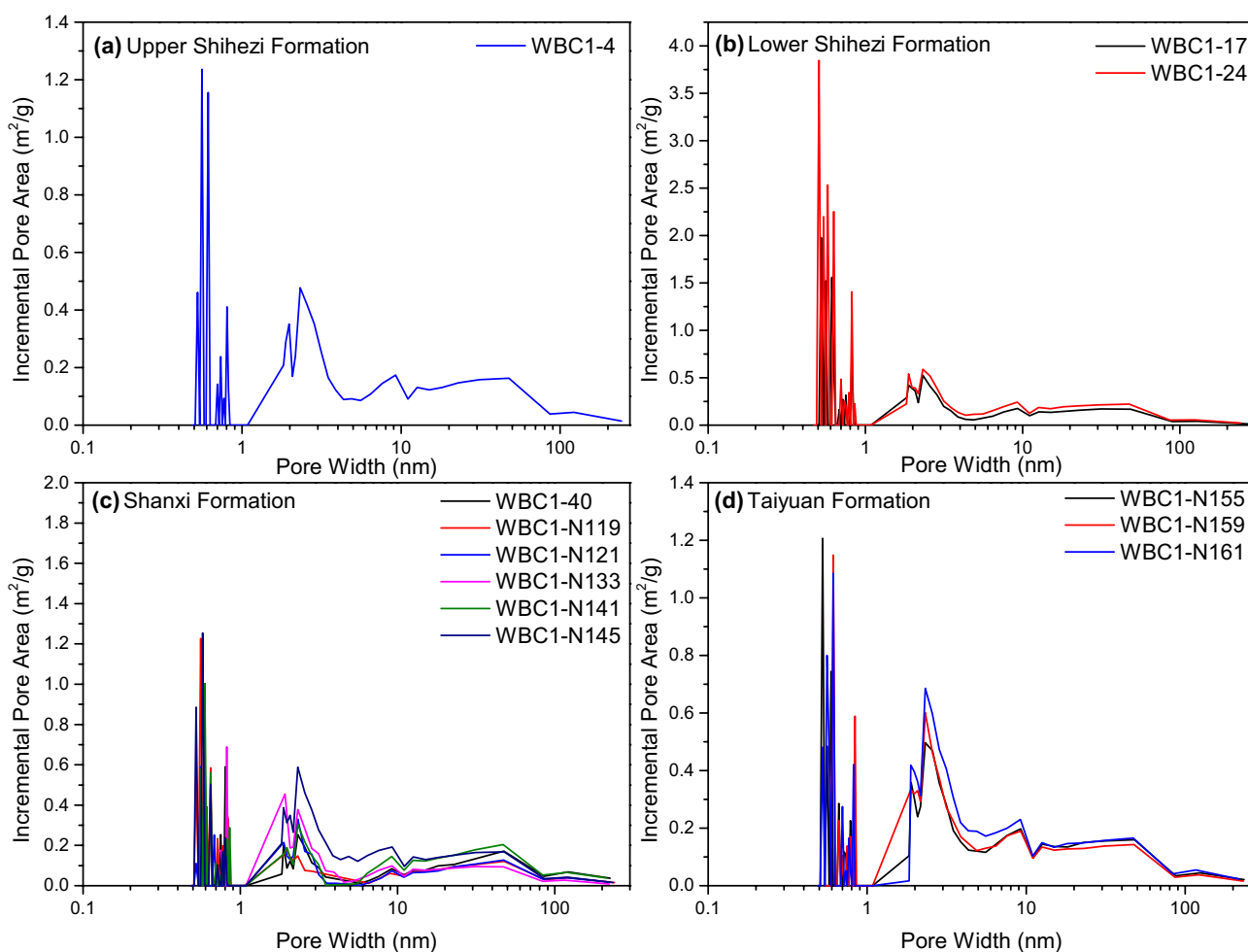$$\ln V = \lambda \cdot \ln \left(\ln \frac{P0}{P} \right) + K$$

Fig. 9 Incremental pore area at different pore widths of shale from different formations (a, b, c and d are Upper Shihezi Formation, Lower Shihezi Formation, Shanxi Formation and Taiyuan Formation, respectively)
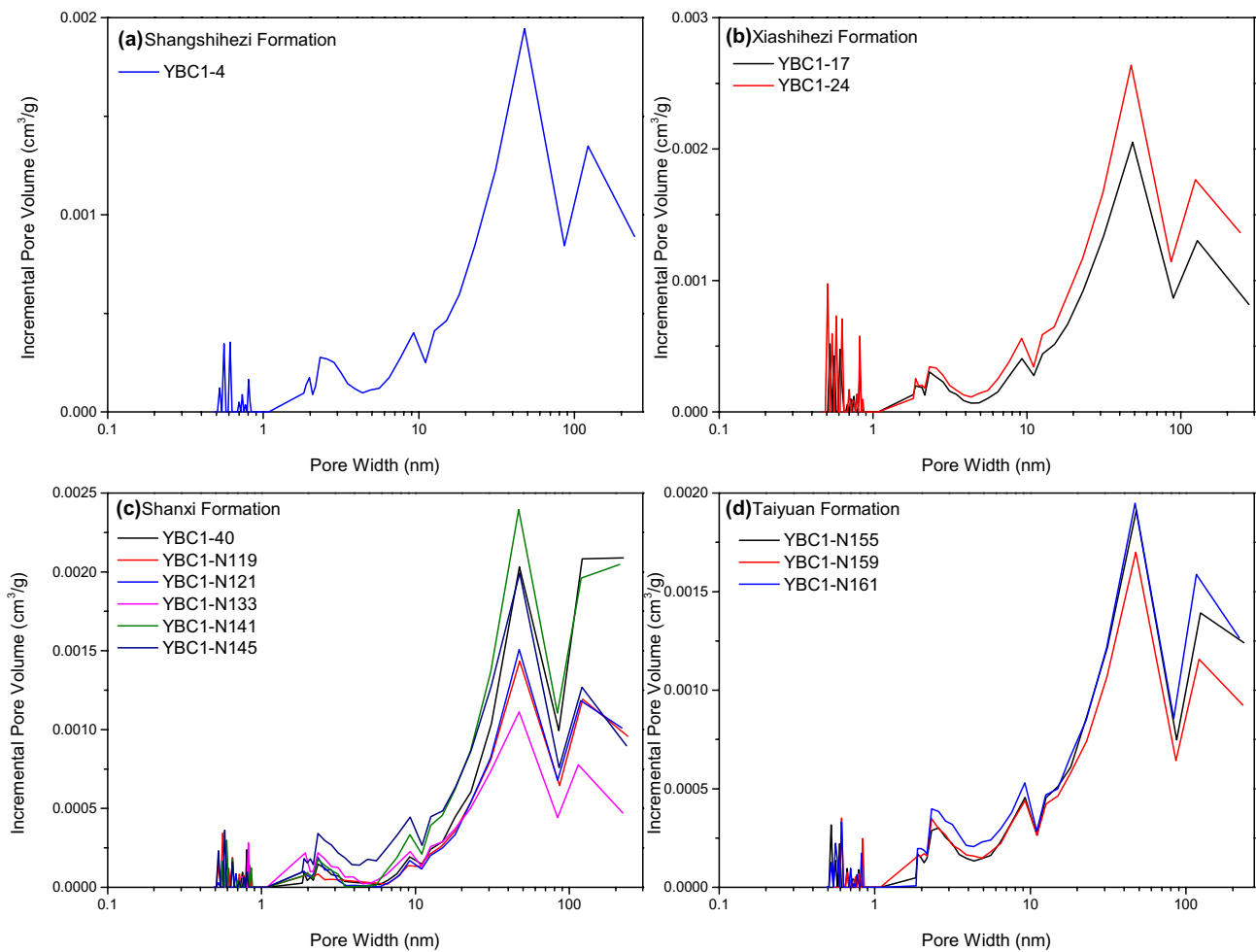
Fig. 10 Incremental pore volume at different pore widths of shale from different formations (**a**, **b**, **c** and **d**) are Upper Shihezi Formation, Lower Shihezi Formation, Shanxi Formation and Taiyuan Formation, respectively)

Table 7 Quantitative specific surface area and pore volume characteristics of the transitional shales

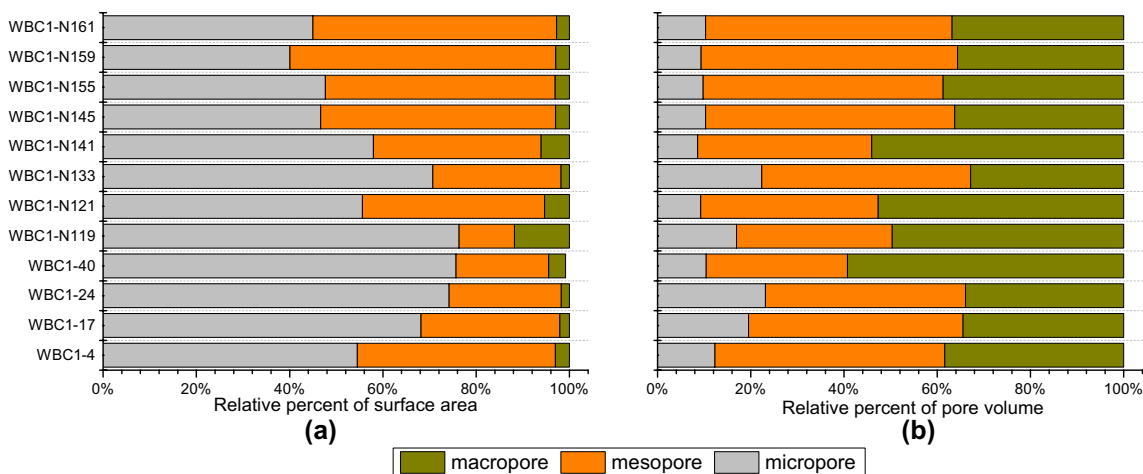| Samples	Specific surface area (m²/g)				Pore volume (cm³/g)			
	Total	Micropore	Mesopore	Macropore	Total	Micropore	Mesopore	macropore
WBC1-4	8.6392	4.7088	3.6696	0.2608	0.0131	0.0016	0.0064	0.0050
WBC1-17	12.6005	8.5894	3.7510	0.2601	0.0146	0.0028	0.0067	0.0050
WBC1-24	20.0978	14.9121	4.8318	0.3540	0.0204	0.0047	0.0087	0.0069
WBC1-40	5.7195	4.3274	1.1370	0.2058	0.0121	0.0013	0.0037	0.0072
WBC1-N119	5.6701	4.3274	0.6730	0.6698	0.0085	0.0014	0.0028	0.0042
WBC1-N121	4.0911	2.2749	1.5977	0.2185	0.0083	0.0008	0.0032	0.0044
WBC1-N133	8.3453	5.9016	2.2929	0.1509	0.0085	0.0019	0.0038	0.0028
WBC1-N141	5.9456	3.4466	2.1373	0.3618	0.0139	0.0012	0.0052	0.0075
WBC1-N145	8.7619	4.0860	4.4154	0.2606	0.0136	0.0014	0.0073	0.0049
WBC1-N155	8.4256	4.0150	4.1509	0.2596	0.0137	0.0013	0.0070	0.0053
WBC1-N159	7.6711	3.0736	4.3711	0.2264	0.0124	0.0012	0.0068	0.0044
WBC1-N161	10.2719	4.6206	5.3675	0.2837	0.0154	0.0016	0.0081	0.0057

Fig. 11 Relative percent of **a** specific surface area and **b** pore volume of macropore, mesopore and micropore for shale samples

where V and P_0 represent the equilibrium volume of adsorbed N_2 (cm^3/g) and the saturation pressure of N_2 (MPa), respectively. λ and K are the linear correction coefficient and a constant, respectively. Fractal dimension (D) can be calculated as follows [40–41]:

$$D = \lambda + 3.$$

The calculated FHH fractal dimension (D) for shale samples is presented in Fig. 12 and Table 7. In this calculation, the pressure has been divided into two groups for

linear fitting according to the diverse stages for adsorption isotherm curves: (1) $P/P_0 = 0$–0.5. In the fitting during this pressure, the FHH fractal dimension (D_1) indicates the heterogeneous of surface roughness and pore structure for micropore at low pressure; (2) $P/P_0 = 0.5$–1. In the fitting during this pressure, the FHH fractal dimension (D_2) indicates the heterogeneous of main pore structure and relative great pores at higher pressure. It is well accepted that N_2 is characterized by different adsorption approaches at varying pressure. Previous studies reveal

Fig. 12 The selective results of fractal dimensions from sample **a** YBC1-4, **b** YBC1-24, (**c**) YBC1-40 and (**d**) YBC1-N159
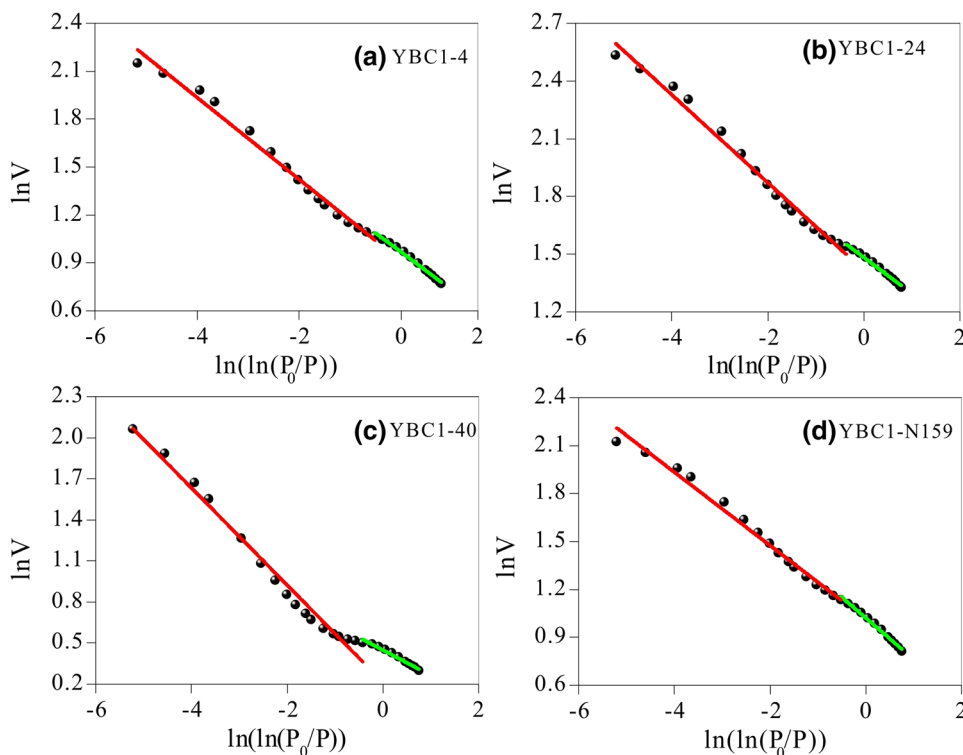
the N_2 adsorption in low pressure ($P/P_0 = 0$–0.5) was controlled by the Van der Waals force, indicating that the D_1, obtained from $P/P_0 = 0$–0.5, can act as the indicator for the roughness of pore surface (Shang et al. 2020; Wang et al. 2016), whereas the N_2 adsorption in relative high pressure ($P/P_0 = 0.5$–1) is influenced by multilayer adsorption, revealing that the D_2, obtained from $P/P_0 = 0.5$–1, can act as the indicator for the irregularity of pore system (Shang et al. 2020; Wang et al. 2016).

Fractal dimension can reflect and characterize the fractal patterns by quantifying their complexity. The fractal dimension increases as the irregular geometric of shale pore structure becomes more complex. The calculated fractal dimension in this study is presented in Table 8, the results show that D_1 ranges from 2.7006 to 2.8493 (average = 2.7666), whereas D_2 ranges from 2.6452 to 2.7958 (average = 2.7254). It is obvious that D_2 is generally less than D_1, indicating that the surface roughness and micropore irregularity of the pore system of transitional shale are slightly stronger than the heterogeneity of the whole pore structure. Compared with the transitional facies shale in other basins, the fractal dimension of shale samples in FB area is significantly higher than that of Dalong Formation in Lower Yangtze Platform (D ranges from 2.511 to 2.619) (Xu et al. 2020) and Shihezi Formation in Huainan coalfield (D_1 ranges from 2.4750 to 2.6104) (Bu et al. 2015) and slightly higher than that of Niutitang and Longmaxi Formation in Lower Cambrian strata (Hu et al. 2016; Xi et al. 2018). Hence, the result may suggest that the surface roughness and pore structure heterogeneity of shale samples in this study is more complex compared to other marine–continental transitional shale.

Influencing factors of CH_4 adsorption for the transitional shales

Pore structure

The relationship of SSA and PV with Langmuir volume is presented in Fig. 13. The results indicate that the total SSA and total PV, obtained from the BJH model in N_2 adsorption experiment and DFT model in CO_2 adsorption experiment, are positively correlated with Langmuir volume. The R^2 of liner fitting for total SSA and total PV is 0.9669 and 0.723, respectively. But the V_L increased with an almost constant value of SSA and PV of macropore, indicating that the macropore almost cannot influence the methane adsorption in shale matrix. In addition, unobvious positive relationship can be discovered of SSA and PV of mesopore with Langmuir volume. However, positive correlation can be observed of SSA and PV of micropore with Langmuir volume. The R^2 of liner fitting for micropore SSA and total PV is 0.9228 and 0.9505, respectively. Hence, the experimental results reveal that the micropore SSA and total PV can obviously influence the transitional shale methane adsorption capacity. Furthermore, the micropore SSA may have a greater impact on the methane adsorption capacity than micropore PV.

Pore structure parameters, mainly including pore size distribution, can influence the adsorption force between the pore walls and adsorbed gas molecules (Burggraaf 1999; Chen et al. 2019; Cui et al. 2004; Wang and Jin 2019). Generally, the adsorption force between gas molecules and pore walls decreased with increasing pore width (Burggraaf 1999; Cui et al. 2004). During the adsorption of methane on shale matrix after hydrocarbon generation, the physical adsorption acts as the leading pattern and controlled by Van der Waals force (Kumar et al. 2015; Tao and Rappe 2014; Zhua et al. 2016). Therefore, the adsorption force of CH_4 on the shale matrix decreases with increasing pore width. Hence,

Table 8 Fractal dimensions of transitional shale samples from Well WBC1

| Samples	Formation	$P/P_0 (0-0.5)$			$P/P_0 (0.5-1)$		
		λ_1	R^2	$D_1 = 3 + \lambda_1$	λ_2	R^2	$D_2 = 3 + \lambda_2$
WBC1-4	Upper Shihezi	−0.2493	0.9939	2.7507	−0.2563	0.9840	2.7437
WBC1-17	Lower Shihezi	−0.1648	0.9864	2.8352	−0.2042	0.9835	2.7958
WBC1-24	Lower Shihezi	−0.1876	0.9901	2.8124	−0.2309	0.9894	2.7691
WBC1-40	Shanxi	−0.2013	0.9934	2.7987	−0.3548	0.9835	2.6452
WBC1-N119	Shanxi	−0.1507	0.9285	2.8493	−0.3459	0.9801	2.6541
WBC1-N121	Shanxi	−0.2326	0.9709	2.7674	−0.3337	0.9823	2.6663
WBC1-N133	Shanxi	−0.2926	0.9890	2.7074	−0.2684	0.9874	2.7316
WBC1-N141	Shanxi	−0.1542	0.9910	2.8458	−0.3099	0.9878	2.6901
WBC1-N145	Shanxi	−0.2994	0.9916	2.7006	−0.2585	0.9866	2.7415
WBC1-N155	Taiyuan	−0.2951	0.9939	2.7049	−0.2637	0.9887	2.7363
WBC1-N159	Taiyuan	−0.2690	0.9931	2.7310	−0.2297	0.9887	2.7703
WBC1-N161	Taiyuan	−0.3044	0.9956	2.6956	−0.2395	0.9945	2.7605
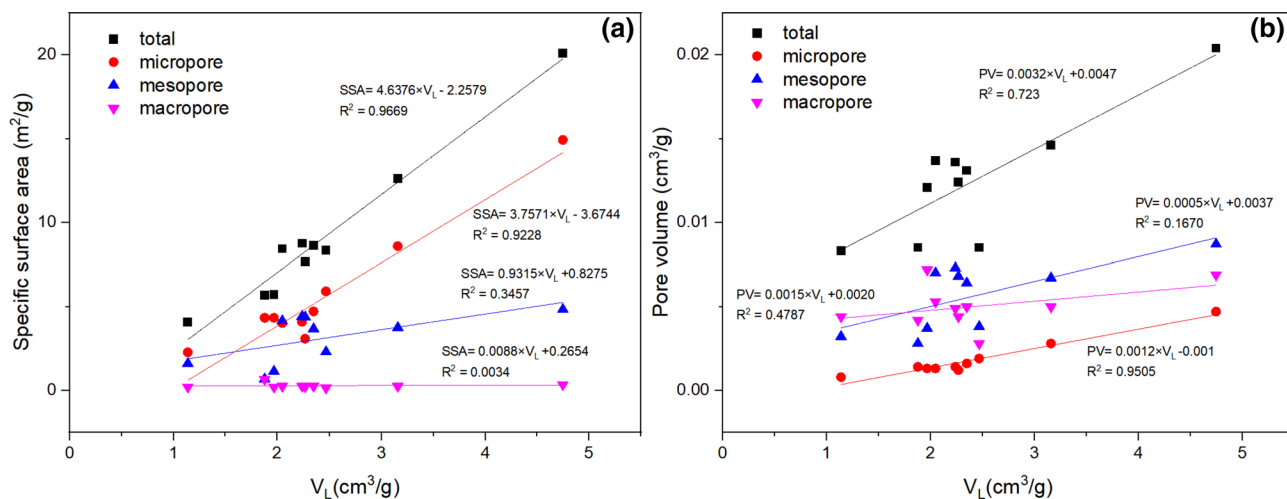
Fig. 13 The correction between specific surface area **a** and pore volume **b** of BJH model with Langmuir volume
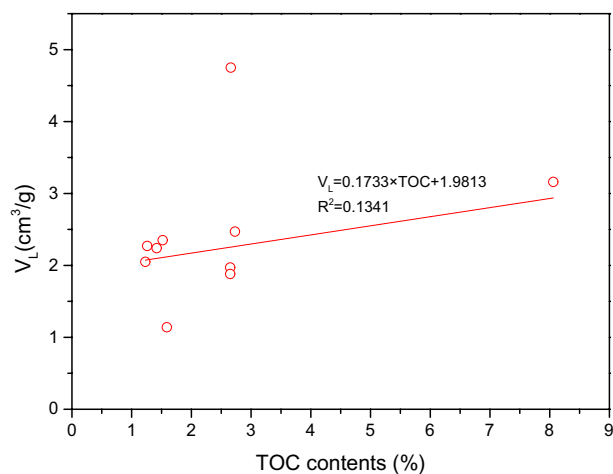

Fig. 14 Relationship between Langmuir volume and TOC content

the pore structure parameters of micropore are the primary factor affecting adsorption capacity of CH4 for transitional shale in this study.

TOC contents

The relationship between SSA and TOC contents indicates that the organic pores were not well developed in marine–continental transitional shale. The experiments reveal that the inorganic pore mainly contributed to the pore structure. Based on this, the relationship between Langmuir volume and TOC content is presented in Fig. 14. The results reveal that the V_L was unobvious positive correlated with TOC ($R^2 = 0.0564$), indicating that the organic matters almost rarely contribute to adsorption capacity of CH4 from the shale samples.

Previous studies have investigated the relationship between the V_L and TOC content for shale from different petroliferous basins (Han et al. 2020; He et al. 2019b; Li et al. 2019; Tan et al. 2014; Wang et al. 2019; Yang et al. 2016a), the results indicate that a positive correlation between adsorption capacity of CH_4 and TOC contents can be observed. However, the experimental results in this study reveal that the adsorption capacity of CH_4 is not related to the organic matters, may suggesting that the adsorption capacity of CH_4 can be controlled by other factors.

Mineral compositions

Previous studies reveal that the clay minerals can affect adsorption capacity of CH_4 (Liu et al. 2013). In addition, hydrocarbons can absorb onto the surface of the carbonate mineral (Liu et al. 2019a; Suess 1970; Zullig and Morse 1988). Moreover, quartz is of low adsorption capacity of methane due to the fact that quartz has no pore structure.

The relationship between Langmuir volume and mineral compositions is presented in Fig. 15. The results show that the V_L is of negative correlated to the contents of quartz, suggesting that high content of quartz can dilute the remaining mineral components that can absorb methane (Fig. 15a). However, positive correlation can be discovered between Langmuir volume (V_L) and clay contents (Fig. 15b). Meanwhile, no positive relationship of Langmuir volume (V_L) and Muscovite and Feldspar can be observed. Hence, the experimental results indicate that clay minerals act as the leading factor influencing the adsorption capacity of CH4 from the transitional shale samples in this study.
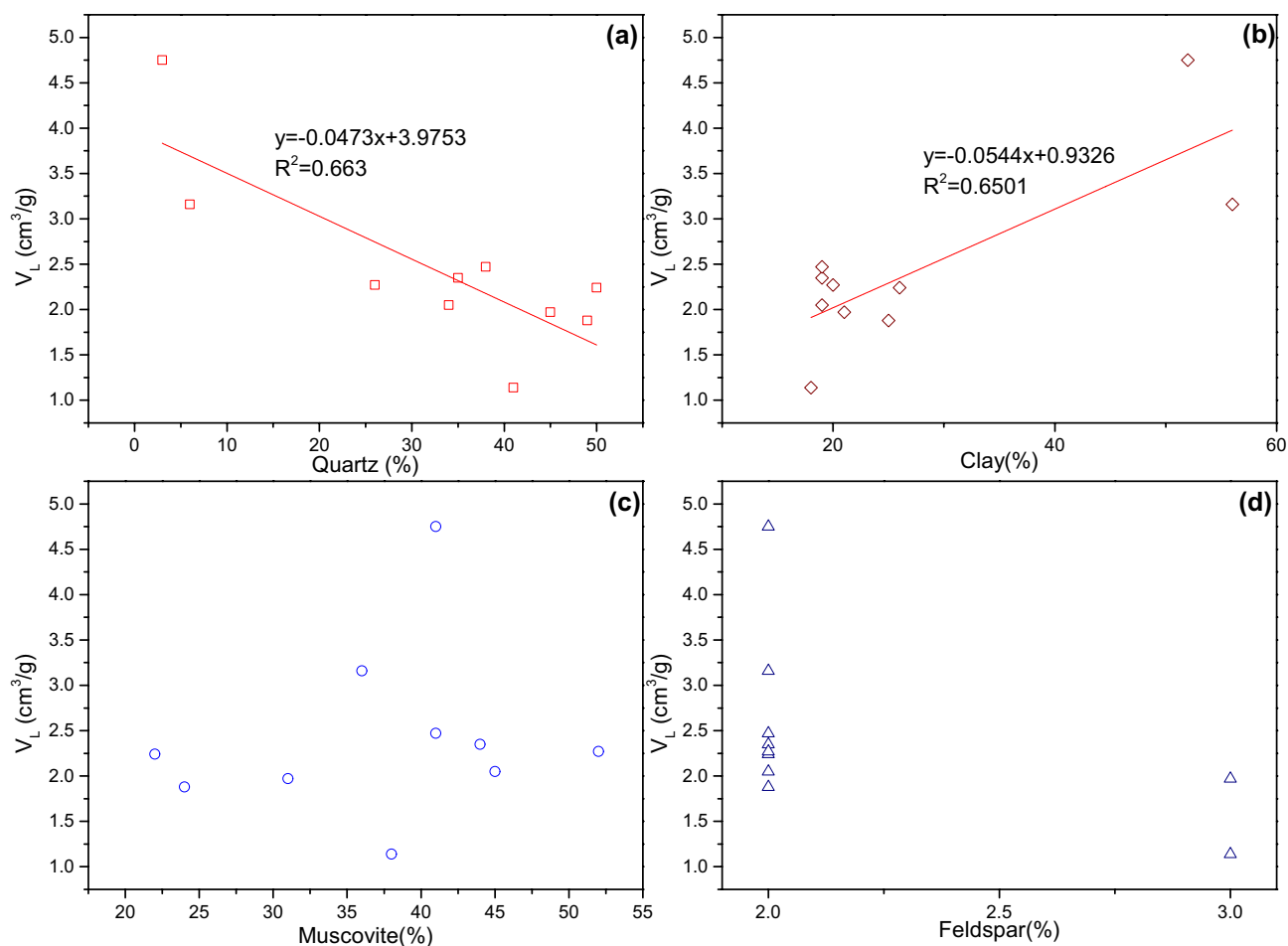
Fig. 15 Relationship between Langmuir volume and mineral compositions (**a**) quartz; (2) clay; (3) muscovite; (4) feldspar)

Summary and conclusions

In this study, a series of experiments were conducted to investigate the pore structure and adsorption capacity of methane from transitional shale from the SNCB. Based on this, the pore structure characteristics and fractal dimension were studied. Moreover, the influencing factors of CH_4 adsorption for the transitional shales were analyzed. The major conclusion can be listed as follows:

(1) Inorganic pores are the main component of pore network in the transitional shale from the southern North China basin;
(2) Micropore has a greater impact on the adsorption capacity of methane than mesopore and macropore in the transitional shale from the SNCB;
(3) Different from shales in other petroliferous basin, clay minerals are primary factor affecting adsorption capacity of methane for transitional shale in this study;
(4) The pore network in the transitional shale for this study is characterized by greater fractal dimensions and more

heterogeneous pore network compared to other marine–continental transitional shales.

However, it must be pointed out that the above conclusions are only for the transitional facies shales of SNCB. The transition shales in other basins or areas may have different pore structure features and adsorption properties due to the possible differences in physical and chemical character.

References

Anees A, Shi WZ, Ashraf U, Xu QH (2019) Channel identification using 3D seismic attributes and well logging in lower Shihezi formation of Hangjinqi area, northern Ordos Basin. China J Appl Geophys 163:139–150

Avnir D, Jaroniec M (1989) An isotherm equation for adsorption on fractal surfaces of heterogeneous porous materials. Langmuir 5:1431–1433

Bu HL, Ju YW, Tan JQ, Wang GC, Li XS (2015) Fractal characteristics of pores in non-marine shales from the Huainan coalfield, eastern China. J Nat Gas Sci Eng 24:166–177

Burggraaf AJ (1999) Single gas permeation of thin zeolite (MFI) membranes: theory and analysis of experimental observations. J Membr Sci 155:45–65

Cao TT, Song ZG, Wang SB, Xia J (2016) Characterization of pore structure and fractal dimension of Paleozoic shales from the northeastern Sichuan Basin. China J Nat Gas Sci Eng 35:882–895

Cao Z, Jiang H, Zeng J, Saibi H, Zhou G (2020) Nanoscale liquid hydrocarbon adsorption on clay minerals: a molecular dynamics simulation of shale oils. Chem Eng J

Chen G, Lu S, Liu K, Xue Q, Qi Q (2019) Investigation of pore size effects on adsorption behavior of shale gas. Mar Pet Geol 109:1–8

Cui X, Bustin RM, Dipple G (2004) Selective transport of CO2, CH4, and N2 in coals: insights from modeling of experimental gas adsorption data. Fuel 83:293–303

Dang W, Zhang J, Wei X, Tang X, Chen Q, Li Z, Zhang M, Liu J (2017) Geological controls on methane adsorption capacity of lower Permian transitional black shales in the Southern North China Basin, Central China: experimental results and geological implications. J Pet Sci Eng 152:456–470

Gasparik M, Ghanizadeh A, Bertier P, Gensterblum Y, Bouw S, Krooss BM (2012) High-pressure methane sorption isotherms of black shales from The Netherlands. Energy Fuels 26:4995–5004

Guo RL, Xie QC, Qu XF, Chu MJ, Li ST, Ma DX, Ma XF (2020) Fractal characteristics of pore-throat structure and permeability estimation of tight sandstone reservoirs: a case study of Chang 7 of the upper triassic Yanchang formation in Longdong area, Ordos Basin. China J Pet Sci Eng 184:13

Han H, Pang P, Zhong NN, Luo QY, Ma Y, Gao Y (2020) The pore characteristics and gas potential of the jurassic continental shales in the middle-small basins, northwest China. J Pet Sci Eng 188:13

He L, Mei HY, Hu XR, Dejam M, Kou ZH, Zhang ML (2019a) Advanced flowing material balance to determine original gas in place of Shale gas considering adsorption hysteresis. SPE Reserv Eval Eng 22:1282–1292

He Q, Dong T, He S, Zhai GY (2019b) Methane adsorption capacity of marine-continental transitional facies shales: the case study of the upper Permian longtan formation, northern Guizhou Province Southwest China. J Pet Sci Eng 183:15

Hill DG, Nelson CR (2000) Gas productive fractured shales: an overview and update. Gas Tips 6(3):4–13

Hu JG, Tang SH, Zhang SH (2016) Investigation of pore structure and fractal characteristics of the lower silurian longmaxi shales in western Hunan and Hubei Provinces in China. J Nat Gas Sci Eng 28:522–535

Huang Z, Gao C, Ji R (2005) Analysis of evolution of Meso-Cenozoic basins in southern North China. Oil Gas Geol 26:252–256

Jaroniec M (1995) Evaluation of the fractal dimension from a single adsorption isotherm. Langmuir 11:2316–2317

Kuila U, Prasad M (2013) Specific surface area and pore-size distribution in clays and shales. Geophys Prospect 61:341–362

Kumar KV, Charalambopoulou G, Kainourgiakis M, Stubos A, Steriotis T (2015) Insights on the physical adsorption of hydrogen and methane in UiO series of MOFs using molecular simulations. Comput Theor Chem 1061:36–45

Law BE, Curtis JB (2002) Introduction to unconventional petroleum systems. AAPG Bull 86:1851–1852

Li XF, Liu P, Liu R (2019) Methane adsorption characteristics of shale from different basins and its geological significance. Pet Sci Technol 37:261–267

Liang C, Jiang ZX, Cao YC, Zhang JC, Guo L (2017) Sedimentary characteristics and paleoenvironment of shale in the Wufeng-Longmaxi formation, North Guizhou Province, and its shale gas potential. J Earth Sci 28:1020–1031

Liu D, Yuan P, Liu H, Li T, Tan D, Yuan W, He H (2013) High-pressure adsorption of methane on montmorillonite, kaolinite and illite. Appl Clay Sci 85:25–30

Liu Y, Zhang JC, Tang X (2016) Predicting the proportion of free and adsorbed gas by isotopic geochemical data: a case study from lower Permian shale in the southern North China basin (SNCB). Int J Coal Geol 156:25–35

Liu P, Wang X, Meng Q, Wang X, Zhang L, Liu C, Lei Y, Jiang C, Yin J (2018a) Simulation of shale gas generation by using different experimental systems: a case study from Chang7 shale in the Ordos Basin. J Nat Gas Sci Eng 49:169–178

Liu Y, Tang X, Zhang J, Mo X, Huang H, Liu Z (2018b) Geochemical characteristics of the extremely high thermal maturity transitional shale gas in the Southern North China Basin (SNCB) and its differences with marine shale gas. Int J Coal Geol 194:33–44

Liu P, Wang X, Horita J, Fang X, Zheng J, Li X, Meng Q (2019a) Evaluation of total organic carbon contents in carbonate source rocks by modified acid treatment method and the geological significance of acid-soluble organic matters. Energy Explor Exploit 37:219–229

Liu P, Wang XF, Li XF, Zhang T, Liu WH (2019b) Geochemical characteristics of released organic matters by acid decomposition of hydrocarbon source rocks from different sedimentary basins. Geofluids 2019:12

Liu P, Wang X, Lin Y, Liu C, Li X, Liu W (2020) Chemical and carbon isotope fractionations of alkane gases desorbed from confined systems and the application toward shale gas reservoir. Mar Pet Geol 113:104103

Liu P, Wang XF, Li XF, Zhang T, Du GC, Liu WH (2020b) Competitive adsorption characteristics of CH4/C2H6 gas mixtures on model substances, coal and shale. Fuel 279:9

Loucks RG, Reed RM, Ruppel SC, Hammes U (2012) Spectrum of pore types and networks in mudrocks and a descriptive classification for matrix-related mudrock pores. AAPG Bull 96:1071–1098

Mangi HN, Yan DT, Hameed N, Ashraf U, Rajper RH (2020) Pore structure characteristics and fractal dimension analysis of low rank coal in the lower Indus Basin, SE Pakistan. J Nat Gas Sci Eng 77:13

Martini AM, Walter LM, Budai JM, Ku T, Kaiser CJ, Schoell M (1998) Genetic and temporal relations between formation waters and biogenic methane: upper Devonian Antrim Shale, Michigan Basin, USA. Geochim Cosmochim Acta 62:1699–1720

Peters KE, Walters CC, Moldowan JM (2004) The biomarker guide: biomarkers and isotopes in petroleum systems and earth history

Pfeifer P, Avnir D (1983) Chemistry in noninteger dimensions between two and three. I. Fractal theory of heterogeneous surfaces. J Chem Phys 79:3558–3565

Springer

Qiu XD, Yang H, Dejam M, Tan SP, Adidharma H (2021) Experiments on the capillary condensation/evaporation hysteresis of pure fluids and binary mixtures in cylindrical nanopores. J Phys Chem C 125:5802–5815

Rouquerol J, Avnir D, Fairbridge CW, Everett DH (1994) Recommendations for the characterization of porous solids (Technical Report). Pure Appl Chem 66P:1739–1758

Shang FH, Zhu YM, Gao HT, Wang Y, Liu RY (2020) Relationship between tectonism and composition and pore characteristics of shale reservoirs. Geofluids 2020:14

Sing KSW (1982) Reporting physisorption data for gas/solid systems. Pure Appl Chem 54(11):2201–2218

Suess E (1970) Interaction of organic compounds with calcium carbonate—I. Association phenomena and geochemical implications. Geochim Cosmochim Acta 34:157–168

Sun M, Yu B, Hu Q, Chen S, Xia W, Ye R (2016) Nanoscale pore characteristics of the lower cambrian niutitang formation shale: a case study from well Yuke #1 in the Southeast of Chongqing, China. Int J Coal Geol 154–155:16–29

Tan JQ, Weniger P, Krooss B, Merkel A, Horsfield B, Zhang JC, Boreham CJ, van Graas G, Tocher BA (2014) Shale gas potential of the major marine shale formations in the upper Yangtze platform, South China, Part II: methane sorption capacity. Fuel 129:204–218

Tang S, Zhan J, Elsworth D, Tang X, Li Z, Du X, Yang X (2016) Lithofacies and pore characterization of the lower Permian Shanxi and Taiyuan shales in the southern North China Basin. J Nat Gas Sci Eng 36:644–661

Tao J, Rappe AM (2014) Physical adsorption: theory of van der waals interactions between particles and clean surfaces. Phys Rev Lett 112(10):106101

Wang Y, Jin Z (2019) Effect of pore size distribution on hydrocarbon mixtures adsorption in shale nanoporous media from engineering density functional theory. Fuel 254:115650

Wang GC, Ju YW, Bao Y, Yan ZF, Li XS, Bu HL, Li QG (2014) Coal-bearing organic shale geological evaluation of Huainan-Huaibei coalfield, China. Energy Fuels 28:5031–5042

Wang G, Ju Y, Yan Z, Li Q (2015) Pore structure characteristics of coal-bearing shale using fluid invasion methods: a case study in the Huainan-Huaibei Coalfield in China. Mar Pet Geol 62:1–13

Wang Y, Zhu YM, Liu SM, Zhang R (2016) Pore characterization and its impact on methane adsorption capacity for organic-rich marine shales. Fuel 181:227–237

Wang Y, Liu LF, Sheng Y, Wang XM, Zheng SS, Luo ZH (2019) Investigation of supercritical methane adsorption of overmature shale in Wufeng-Longmaxi formation, Southern Sichuan Basin, China. Energy Fuels 33:2078–2089

Wang B, Xu Q, Wang Y, Liu E, Shi D (2020) Sturctural characteristic of the faults in the southern North China Basin and its relationship with petroleum exploration. Chin J Geol 55:109–121

Xi ZD, Tang SH, Wang J, Yi JJ, Guo YY, Wang KF (2018) Pore structure and fractal characteristics of Niutitang shale from China. Minerals 8:18

Xu H, Zhao Z, Yang Y, Tang Z (2003) Structural pattern and structural style of the Southern North China Basin. Acta Geosci Sin 24:27–33

Xu LF, Zhang JC, Ding JH, Liu T, Shi G, Li XQ, Dang W, Cheng YS, Guo RB (2020) Pore structure and fractal characteristics of different shale Lithofacies in the Dalong formation in the Western area of the lower Yangtze platform. Minerals 10:25

Yang R, He S, Hu QH, Hu DF, Zhang SW, Yi JZ (2016a) Pore characterization and methane sorption capacity of over-mature organic-rich Wufeng and Longmaxi shales in the southeast Sichuan Basin, China. Mar Pet Geol 77:247–261

Yang R, He S, Yi JZ, Hu QH (2016b) Nano-scale pore structure and fractal dimension of organic-rich Wufeng-Longmaxi shale from Jiaoshiba area, Sichuan Basin: investigations using FE-SEM, gas adsorption and helium pycnometry. Mar Pet Geol 70:27–45

Yu H, Lv F, Guo Q, Lu W, Wu J, Han S (2005) Proto-sediment basin types and tectonic evolution in the southern edge of north china plate. Pet Geol Exp 27:111–117

Zhua YQ, Su H, Jing Y, Guo JC, Tang JL (2016) Methane adsorption on the surface of a model of shale: a density functional theory study. Appl Surf Sci 387:379–384

Zou C, Dong D, Wang S, Li J, Li X, Wang Y, Li D, Cheng K (2010) Geological characteristics, formation mechanism and resource potential of shale gas in China. Pet Explor Dev 37:641–653

Zullig JJ, Morse JW (1988) Interaction of organic acids with carbonate mineral surfaces in seawater and related solutions: I Fatty Acid Adsorption. Geochim Cosmochim Acta 52:1667–1678

Publisher's Note Springer Nature remains neutral with regard to jurisdictional claims in published maps and institutional affiliations.